Lower length scale model for palladium attack of silicon carbide in TRISO fuel

INL/RPT-24-80441

Nuclear Energy Advanced Modeling and Simulation (NEAMS)

AUGUST 2024

Chaitanya V. Bhave,
Mathew Swisher,
Larry K. Aagesen,
Jacob A. Hirschhorn, and
Pierre-Clément A. Simon

Idaho National Laboratory

Idaho National Laboratory

Battelle Energy Alliance manages INL for the U.S. Department of Energy's Office of Nuclear Energy

INL/RPT-24-80441

Lower length scale model for palladium attack of silicon carbide in TRISO fuel

Chaitanya V. Bhave,
Mathew Swisher,
Larry K. Aagesen,
Jacob A. Hirschhorn, and
Pierre-Clément A. Simon
Idaho National Laboratory

August 2024

Idaho National Laboratory
Computational Mechanics and Materials Department
Idaho Falls, Idaho 83415

http://www.inl.gov

Prepared for the
U.S. Department of Energy
Office of Nuclear Energy
Under DOE Idaho Operations Office
Contract DE-AC07-05ID14517

Page intentionally left blank

ABSTRACT

TRistructural ISOtropic (TRISO) particle fuels rely on silicon carbide (SiC) as the primary barrier for metallic fission product (FP) release. Palladium (Pd) generated by fission degrades the SiC layer, resulting in the formation of lamellar layers of palladium silicides (Pd_xSi) and carbon (C) perpendicular to the direction of attack. The Pd attack has been hypothesized to be responsible for failure of the SiC layer and enhance FP release. To better understand and quantify Pd attack of SiC in TRISO particles, a multiscale, mechanistic model of Pd transport is being developed by the NEAMS program. Previous work provided an initial hypothesis for modeling lamellar microstructure formation in SiC due to Pd attack using a phase-field model. The work described in this report builds on the previous model by using molecular dynamics (MD) simulations to parameterize the phase-field model kinetics, and build a reduced order model in BISON using the improved mesoscale Pd penetration model.

ACKNOWLEDGMENTS

This report was authored by a contractor of the U.S. Government under Contract DE-AC07-05ID14517. Accordingly, the U.S. Government retains a non-exclusive, royalty-free license to publish or reproduce the published form of this contribution, or allow others to do so, for U.S. Government purposes.

This research made use of the resources of the High Performance Computing Center at Idaho National Laboratory, which is supported by the Office of Nuclear Energy of the U.S. Department of Energy and the Nuclear Science User Facilities under Contract No. DE-AC07-05ID14517.

Page intentionally left blank

CONTENTS

ABSTRACT iii

ACKNOWLEDGMENTS iv

ACRONYMS x

1. INTRODUCTION 1

2. MOLECULAR DYNAMICS 2
   - 2.1. Molecular Dynamics Introduction . . . 2
   - 2.2. Modeling TRISO materials via Molecular Dynamics . . . 2
   - 2.3. Methodology for measuring atomistic scale diffusion . . . 2
   - 2.4. Atomistic Scale Diffusion Mechanisms of Pd . . . 3
   - 2.5. Diffusion of Pd in Graphite . . . 4
   - 2.6. Diffusion of Pd in Silicon Carbide . . . 5
   - 2.7. Atomistic Scale Diffusion Mechanisms of Carbon in Silicon Carbide . . . 7
   - 2.8. Discussion . . . 8

3. PHASE-FIELD MODEL DEVELOPMENT 9
   - 3.1. Phase-field model . . . 9
   - 3.2. Effect of interface energy . . . 10
   - 3.3. Effect of concentrated Pd source . . . 10
   - 3.4. Numerical model development . . . 11
   - 3.5. Discussion . . . 11

4. ENGINEERING SCALE REDUCED ORDER MODEL DEVELOPMENT 15
   - 4.1. Derivation of mechanistic reduced order model . . . 15
   - 4.2. Calculation of flux concentration factor . . . 16
   - 4.3. Validation of ROM . . . 18
   - 4.4. Comparison to empirical BISON model . . . 19
   - 4.5. Discussion . . . 20

5. CONCLUSION 22

6. REFERENCES 23

FIGURES

Figure 1. Example configurations from Pd diffusion in graphite at 1473K for intraplanar diffusion (a) and grain boundary diffusion (b). Carbon atoms are shown in red and Pd atoms are shown in yellow. In figure a, the diffusion of Pd atoms is blocked in the up/down direction by layers of carbon, but can diffuse in the plane indicated by the blue arrows. In figure b, carbon atoms in a perfect graphite crystal structure have been removed from the the polycrystalline graphite structure to improve clarity. . . . 4

Figure 2. Diffusivity of Pd atoms in β-SiC obtained from MD simulations for grain boundary mechanism and substitutional mechanisms. The shaded region indicates the standard deviation in the measurement of the diffusivity taken from 10 simulations. 6
Figure 3. Average diffusivity of carbon atoms in β-SiC obtained from MD simulations performed at temperatures between 1100K and 1818K. The shaded region indicates the standard deviation diffusivity taken from 10 simulations. 8
Figure 4. Effect of interface energy on lamellar width of Pd_2Si formed after exposure to a Pd flux of 10 pmol/m^2/s for 2 years. 11
Figure 5. Effect of uniform and concentrated Pd flux sources on microstructure evolution of SiC. The red region denotes graphite phase, blue region denotes SiC, and the gray region denotes Pd_2Si. (a) Initial microstructure consists of SiC with an initial 100 nm layer of graphite (red). (b) Final microstructure (t=2 years) after a uniform Pd flux of 10 pmol/m^2/s on the left boundary. (c) Final microstructure (t=2 years) after a concentrated Pd flux of 500 pmol/m^2/s through a 4 nm region on left boundary. 12
Figure 6. Phase diagram calculation for Mo-Ni-Re-Cr system using the sub-lattice Kim-Kim-Suzuki phase-field model implemented using the damped nested solver in Multiphysics Object-Oriented Simulation Environment (MOOSE). (a)-(d) show the atomic fractions of the components. (e) shows the stable phases calculated based on the composition and interface energy by solving the Allen-Cahn equation based on the local composition. Phase IDs 1,2,3,4 signify the phases FCC, BCC, σ, and HCP each respectively. 14
Figure 7. Comparison of 2D diffusion simulation results against analytical expression for flux enhancement factor f. (a) shows the grain boundaries, as indicated by the value of the variable GB, used to interpolate Pd diffusivity in the 2D simulations. (b) compares the results of the steady state diffusion simulation and analytical solution values for f against the grain minor axis size m_i. The 2D simulation points include five values of grain major axis size m_a for each value of m_i, but the points overlap due to the negligible impact of m_a on f. The root mean square percentage error (RMSPE) between the analytical expression and 2D simulation results is 1.4%. (c) and (d) show the steady-state Pd flux along the x and y directions respectively. The flux is higher along the grain boundary (GB)s in the x axis than the grains, and is negligible along the y direction far from the left boundary. 16
Figure 8. Effect of surface temperature and grain minor axis length m_i on Pd penetration depth rate. 19
Figure 9. Comparison of Pd penetration depth prediction over time between empirical fit and mechanistic ROM. (a) Particle power and temperature conditions simulated using BISON (b) Pd flux at IPyC/SiC boundary calculated by BISON, and comparison of empirical and mechanistic ROM penetration depths over time. The empirical ROM predictions only depend on the particle temperature, while the mechanistic ROM predicts a penetration depth dependent on both the particle power history and temperature. 20

TABLES

Table 1. Diffusion data obtained from MD simulations of Pd atoms in graphite. The intraplanar mechanism refers to the diffusion of Pd atoms between layers of graphite, while grain boundary refers to the diffusion of Pd along randomized grain boundaries in polycrystalline graphite. The average diffusivity (D) of 10 simulations and the corresponding standard deviation (σ_D) are provided. 5

Table 2. Diffusion data obtained from MD simulations of Pd atoms in SiC. The interstitial mechanism refers to Pd being an interstitial in SiC, substitutional refers to Pd being placed on a random lattice site, and grain boundary refers to the diffusion rate of Pd along a randomized grain boundary in SiC. The average diffusivity (D) of 10 simulations and the corresponding standard deviation (σ_D) are provided. 6

Page intentionally left blank

ACRONYMS

ABOP	analytical bond-order potential
Ag	silver
C	carbon
CALPHAD	Computer Coupling of Phase Diagrams and Thermochemistry
FP	fission product
GB	grain boundary
INL	Idaho National Laboratory
IPyC	inner pyrolytic carbon
KKS	Kim-Kim-Suzuki
LAMMPS	Large-scale Atomic/Molecular Massively Parallel Simulator
MD	molecular dynamics
MOOSE	Multiphysics Object-Oriented Simulation Environment
MSD	Mean Squared Displacement
NEAMS	Nuclear Energy Advanced Modeling and Simulation
OP	order parameter
OPyC	outer pyrolytic carbon
Pd	palladium
RMSPE	root mean square percentage error
ROM	reduced order model
SiC	silicon carbide
TRISO	TRistructural ISOtropic

Page intentionally left blank

1. INTRODUCTION

TRISO fuel particles are a key component of many advanced nuclear reactor designs due to their robust FP retention capabilities. TRISO particles consist of a fuel kernel at the center, surrounded by a multilayer coating consisting of a porous carbon buffer, inner pyrolytic carbon (IPyC) layer, SiC layer, and an outer pyrolytic carbon (OPyC) layer. These layers protect the physical integrity of the particle and help to contain the FPs produced during reactor operation [1]. In particular, SiC is the main diffusion barrier for metallic FP retention.

While TRISO particles are generally effective at retaining FPs, silver (Ag) is observed to escape during irradiation tests. Existing models for predicting Ag release have generally underestimated the actual release rates and need multiplicative factors greater than 1 to match experimental observations [2]. One potential explanation for this discrepancy is that the presence of Pd may catalyze the release of Ag. Ag and Pd have been found to diffuse together along the grain boundary (GB) in experimental examinations of irradiated TRISO particles [3–5].

Pd a FP formed in the uranium decay chain, which chemically attacks the SiC barrier layer. This reaction produces various palladium silicides and graphitic C, with the stoichiometry shifting towards Pd_2Si at higher temperatures (above 1000°C). This attack is hypothesized to contribute to enhanced FP release, potentially violating fuel design criteria associated with FP retention. A mechanistic understanding of palladium's attack on the SiC barrier layer is crucial for accurately predicting FP release, particularly in advanced reactor designs that aim to push TRISO fuels towards higher burnup. Existing models, like the Pd release model in the BISON fuel performance code, are based on empirical fits to limited experimental data and cannot reliably predict TRISO behavior under operating conditions outside the range from which the fit was derived.

To address this challenge, a mechanistic model is being developed to describe the Pd-SiC interaction and predict its impact on TRISO performance. In previous work, a mesoscale model was established explaining lamellar structure formation during the Pd-SiC reaction [6]. Section 2 details MD simulations performed in this work to provide more accurate Pd diffusivity data for parameterizing the mesoscale model. In section 3, the phase-field model parameterization using the MD diffusivities is described. This model is used to explore the effects of material properties and boundary conditions on Pd penetration depth and microstructure formation. Section 4 details the development of a mechanistic reduced order model (ROM) for Pd penetration depth prediction in BISON using the findings from the mesoscale phase-field model. The new mechanistic ROM is validated against experimental measurements, and also compared against the empirical model in BISON to show the improvement in prediction fidelity. Finally, section 5 provides general conclusions and recommendations for future work.

2. MOLECULAR DYNAMICS

2.1. Molecular Dynamics Introduction

Atomistic modeling is a set of techniques that allows us to build our understanding of the atomic scale phenomena associated with the diffusion of FPs through the different layers of TRISO particles. These lower length scale techniques, such as molecular dynamics (MD), allow us to study both the energetics and kinetics of the transport process, in order to parameterize higher length scale models. Of particular interest is modeling the diffusion behavior of Pd atoms at lower length scales, to fill in gaps in the understanding of the mechanisms affecting the diffusion of Pd inside of TRISO particles.

In this section, we use MD simulations to measure the diffusivity of Pd in both graphite and SiC. The diffusion rate and energetics of these interstitials were measured in both monocrystalline and polycrystalline substrates to determine how grain boundaries influenced the diffusion of FPs. Additional efforts were made to use MD simulations to measure the diffusion rate of carbon self-interstitial atoms in these materials.

2.2. Modeling TRISO materials via Molecular Dynamics

MD is a technique for modeling the behavior of a system consisting of an ensemble of atomic particles using the classical Newtonian equations of motion. The motion of each atom in the simulation is tracked through time by using an interatomic potential to calculate the forces acting upon it, and numerically integrating in time to obtain its position at the next time step of the simulation. In this work, MD simulations were performed using the Large-scale Atomic/Molecular Massively Parallel Simulator (LAMMPS) software, an open source package developed by Sandia National Laboratories [7] that is highly optimized for running MD simulations across many computing cores.

In this atomistic modeling work, we focused on two different material systems that are found in TRISO particles and their interaction of these materials with palladium atoms. The first was a graphite model intended to approximate the behavior of Pd in the buffer and IPyC layers, and the second was β-SiC [8]. The initial atom configurations mono and poly-crystalline materials were generated using the AtomSK software package [9]. To ensure our modeling results are transferable between the different regions of TRISO particles, we used the analytical bond-order potential (ABOP) model for Si-C-Pd created by Chen et al, which was built with the intention of modeling the diffusion of FPs in SiC [10].

2.3. Methodology for measuring atomistic scale diffusion

The primary method for measuring diffusion at atomistic length scales is to utilize the Einstein relation. To calculate the diffusion using this method we utilize the following equation for the diffusion coefficient:

$$D = \frac{r_s^2(t)}{2nt}, \tag{1}$$

where $r_s^2(t)$ is the Mean Squared Displacement (MSD) of the object, t is time, and n is the dimensionality of the system. In the case of atomistic simulations the object being measured can be either a single atom, group of atoms, or another feature of the atomic configuration. However, it is important to carefully consider which atoms are included in order to measure the diffusion rate of the correct atomistic feature. For example,

some features like self-interstitial atoms are not fixed to any specific atom in the simulation, as the interstitial atom can swap with other atoms in the system.

Additionally, the simulations in this work were performed in supercells with a size of at least $16 \times 16 \times 16$ unit cells, to avoid any diffusing atoms from interacting with their own stress field through the periodic boundary conditions. The simulation was equilibrated for 50 ps before starting to track the MSD. MSD measurements were carried out for at least 80 ns and each measurement was replicated 10 times. Replicating the simulations allows for obtaining more sample data and assessing the error in our MSD measurements.

2.4. Atomistic Scale Diffusion Mechanisms of Pd

In order to understand the transport of FPs, such as Pd, through TRISO particles, we need to begin by understanding the underlying mechanisms that govern the transport through each layer of the material. Knowing the mechanisms allows us to have confidence that the atomistic diffusion mechanism we calculate are relevant to the transport process of Pd in the system, while also providing insight into how the material properties and environmental conditions affect this process.

There are two main factors we need to consider when evaluating a diffusion mechanism. The first is the rate at which a given pathway allows for diffusion to occur, and the second is how likely it is for the initial conditions requisite for the mechanism to occur. For the dilute limit where there are only a few Pd atoms located in a supercell of interest, we can estimate the relative likelihood between any two initial conditions by calculating the Boltzmann factor:

$$\frac{p_i}{p_j} = \exp\left(\frac{\epsilon_j - \epsilon_i}{k_b T}\right) \tag{2}$$

Where p_i and p_j are the probabilities of each of the states we are comparing, ϵ_i and ϵ_j are the corresponding energies of each state, k_b is the Boltzmann constant, and T is the temperature. This method assumes that the configuration of atoms is in equilibrium and only evaluates the relative likelihood of the system being in two particular microstates. However, it still provides insight into what configurations are more stable, and we can use those estimates to help inform our analysis of which diffusion mechanisms are most likely to contribute significantly to Pd transport.

2.5. Diffusion of Pd in Graphite

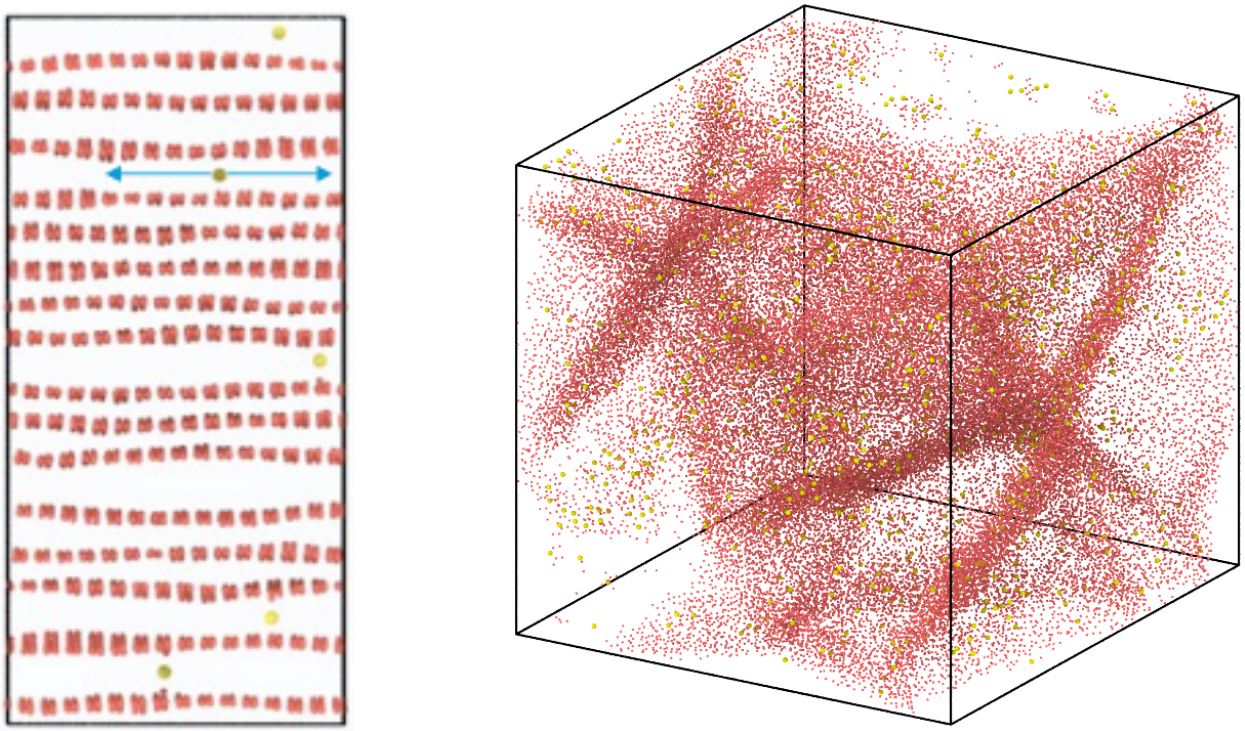

(a) (b)

Figure 1. Example configurations from Pd diffusion in graphite at 1473K for intraplanar diffusion (a) and grain boundary diffusion (b). Carbon atoms are shown in red and Pd atoms are shown in yellow. In figure a, the diffusion of Pd atoms is blocked in the up/down direction by layers of carbon, but can diffuse in the plane indicated by the blue arrows. In figure b, carbon atoms in a perfect graphite crystal structure have been removed from the the polycrystalline graphite structure to improve clarity.

The first combination of materials modeled was the diffusion of Pd in graphite, which serves as an analog for both the buffer and IPyC layers. These layers are both comprised of many different grains of graphite crystals with different orientations, although they differ in the amount of porosity and amorphous carbon included. Due to these similarities we expect the same mechanisms to be present in both layers. The graphite test case also provides the opportunity to validate our methodology by comparing to existing studies in the literature where the diffusion rate of Pd in graphite has been studied experimentally [11].

In order to determine the primary mechanism of Pd diffusion in graphite, two different starting configurations were modeled. The first assumed that the primary method of diffusion was intraplanar Pd diffusion in the gap between layers of carbon. To test this mechanism, a graphite supercell with a size of $72 \times 64 \times 138$ Å^3 was created using the methods described in section 2.2 and allowed to reach equilibrium. Several Pd atoms were then inserted in-between the layers of graphite and the diffusion was measured. An example configuration of the atoms from these simulations is shown in Figure 1a. The diffusion of Pd atoms in this configuration was measured at 1473K, however the diffusion rates were found to be unreasonably high compared to experimental observation. This strongly suggests that diffusion between layers of graphite is not the correct mechanism, and that the Pd atoms located between the graphite layers are in a high energy state that is unlikely to occur. Additionally, measurements showed that the average energy of a Pd interstitial between graphite layers has a

Mechanism	T [K]	D [m^2/s]	σ_D [m^2/s]
Intraplanar	1473	1.2×10^{-6}	0.4×10^{-6}
Grain Boundary	1200	3.4×10^{-14}	1.7×10^{-14}
Grain Boundary	1473	3.7×10^{-12}	2.3×10^{-12}

Table 1. Diffusion data obtained from MD simulations of Pd atoms in graphite. The intraplanar mechanism refers to the diffusion of Pd atoms between layers of graphite, while grain boundary refers to the diffusion of Pd along randomized grain boundaries in polycrystalline graphite. The average diffusivity (D) of 10 simulations and the corresponding standard deviation (σ_D) are provided.

potential energy of -0.63 ± 0.03 eV which indicates this is a high energy state.

Another possible mechanism considered is the diffusion of Pd along grain boundaries in the graphite layer. Large supercells of graphite with size of $140 \times 140 \times 140$ Å^3 were created using AtomSK each containing 3 different cells of equal volumes, randomized boundaries, and randomized crystal orientations. Pd atoms in the interior of each cell is expected to behave similarly to the bulk diffusion case, but the polycrystalline supercell enables us to study the behavior of Pd atoms in the disordered interface between different orientations of graphite crystals. Using these polycrystalline supercells, we were able to measure the formation energy of a Pd atom in the grain boundary, resulting in a potential energy of -4.14 ± 0.02 eV. Evaluating the change in energy between these two configurations using the Boltzmann weight (Equation 2), we can say that Pd will almost always be located along a grain boundary or other areas of the graphite structure containing non-fully bonded carbon atoms.

Further simulations were performed to calculate the diffusion rate of Pd along graphite grain boundaries at 1200K and 1473K. The polycrystalline graphite was equilibrated at the target temperature, Pd atoms were inserted at the grain boundaries, and then the MSD of the Pd atoms was tracked. The resulting diffusion measurements are shown in table 1. The diffusion rate observed along grain boundaries in polycrystalline graphite was found to be within an order of magnitude as experimental results found in the literature of approximately 4.1×10^{-13} m^2/s at a temperature of 1673K [11]. Given the difference in scale between these mechanisms, this strongly suggests that grain boundary diffusion is the correct mechanism for graphite like materials. Additional refinement to investigate the differences in Pd diffusivity between the buffer and IPyC layers would require including more details about the ratio of crystalline graphite to disordered graphite in the material.

2.6. Diffusion of Pd in Silicon Carbide

Of more direct importance to the study of Pd attack on SiC, is using molecular dynamics to fill in the knowledge gaps in the literature about the diffusion mechanisms and diffusion rates of Pd in SiC. Using the same techniques validated against measurement of the diffusion in graphite, we used MD simulations modeling the diffusion of Pd in bulk SiC and along SiC grain boundaries to identify the primary mechanism responsible for diffusion.

In this combination of materials, there are three possible starting conditions that should be considered: bulk diffusion of a Pd interstitial, bulk diffusion of a Pd atom randomly substituted into sites in the SiC lattice, and Pd diffusion along a grain boundary. As before, AtomSK was used to generate the initial configurations of both bulk β-SiC and polycrystalline β-SiC. Simulations of bulk SiC used a simulation cell size of $88 \times 88 \times 88$ Å^3, while the polycrystalline simulations used a cell size of $140 \times 140 \times 140$ Å^3. The configurations were first equilibrated at temperatures of 1200K and 1473K, prior to Pd atoms being inserted to take initial measurements.

Additional measurements were later performed for a range of temperatures between 1100K and 1818K for substitutional and grain boundary diffusion (figure 2).

Mechanism	T [K]	D [m^2/s]	σ_D [m^2/s]
Interstitial	1200	5.2×10^{-13}	1.3×10^{-13}
Interstitial	1473	3.5×10^{-12}	$.6 \times 10^{-12}$
Substitutional	1200	1.8×10^{-16}	0.7×10^{-16}
Substitutional	1473	2.1×10^{-16}	0.5×10^{-16}
Grain Boundary	1200	7.0×10^{-13}	0.5×10^{-13}
Grain Boundary	1473	7.3×10^{-13}	0.7×10^{-13}

Table 2. Diffusion data obtained from MD simulations of Pd atoms in SiC. The interstitial mechanism refers to Pd being an interstitial in SiC, substitutional refers to Pd being placed on a random lattice site, and grain boundary refers to the diffusion rate of Pd along a randomized grain boundary in SiC. The average diffusivity (D) of 10 simulations and the corresponding standard deviation (σ_D) are provided.

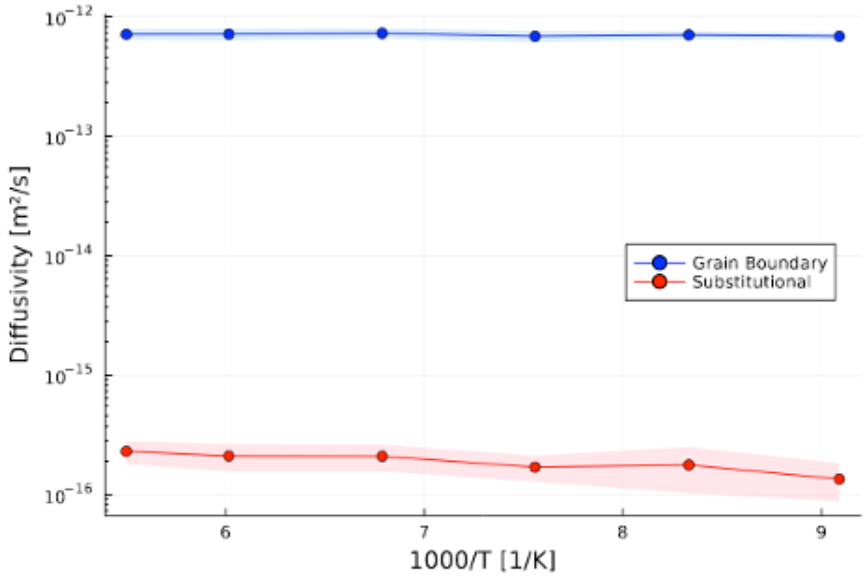

Figure 2. Diffusivity of Pd atoms in β-SiC obtained from MD simulations for grain boundary mechanism and substitutional mechanisms. The shaded region indicates the standard deviation in the measurement of the diffusivity taken from 10 simulations.

Initial simulations were performed to evaluate the formation energy of a Pd atom being in each of the three identified configurations. The diffusion rate for each mechanism was measured at temperatures of 1200K and 1473K, and the resulting diffusion rates are shown in table 2. These results show that Pd can diffuse through SiC at similar rates either along grain boundaries or as an interstitial in the SiC matrix. However, we can also observe from this data that the grain boundary and interstitial diffusion mechanisms scale differently with temperature. The grain boundary mechanism increases by a factor six times less than the interstitial mechanism when going from 1200K to 1473K. The primary difference in these two cases is that the Pd atoms at the grain boundary are able to form strong chemical bonds with the surrounding Si and C atoms. The weak response to temperature would suggest that the available thermal energy in the system is not large enough to break these chemical bonds with any regularity. However, the formation energy for a Pd atom to be placed as

an interstitial is very high, approximately 3.9 eV greater than being located on a grain boundary. This suggests that Pd interstitials would only be created through irradiation and would quickly find a grain boundary or other sink.

On the other hand, Pd atoms will have a significantly lower rate of diffusion if placed on a random site in the lattice structure. Simulations of the diffusion of substitutional Pd atoms showed that the species of the atom the Pd atom replaces does not have a significant effect, because the Pd atom immediately diffuses to a neighboring carbon site in the lattice structure. While inserting the Pd atom into the lattice results in the lowest energy configuration for the Pd atom, this process occurring would also require a low energy location in close proximity for the displaced atom to move into. This chain of events is possible when there are nearby defects in the crystal structure, such as a grain boundary or vacancies created due to irradiation. On the other hand, if we assumed a perfect graphite crystal structure, Pd atoms would be much more likely to be located at the grain boundaries in SiC. Unfortunately this leaves the dominant mechanism open to interpretation, since both mechanisms are feasible. This finding also emphasizes the importance of understanding the complex interaction between Pd, Si, and C at grain boundaries, since a small change in the predicted mechanism would have an outsized impact on the predicted diffusion rate of Pd atoms.

2.7. Atomistic Scale Diffusion Mechanisms of Carbon in Silicon Carbide

Additional work was also performed to measure the rate of diffusion of carbon in SiC, to provide additional information for higher length scale modeling work. The most straightforward measurement of the transport of carbon is to measure the diffusion rate of all the carbon atoms contained in the SiC matrix. MD simulations were performed to measure the MSD of carbon atoms using the same starting configurations for bulk SiC as the previous section at a range of temperatures between 1100K and 1818K. The results of these measurements are shown in figure 3. Unlike the previous cases, we know a priori that the vast majority of carbon atoms are located in the matrix and are not along the grain boundary. While we can use molecular dynamics to estimate the diffusion rate of carbon atoms along SiC grain boundaries, it is much more computationally expensive measurement and there is not currently a need for this specific parameter.

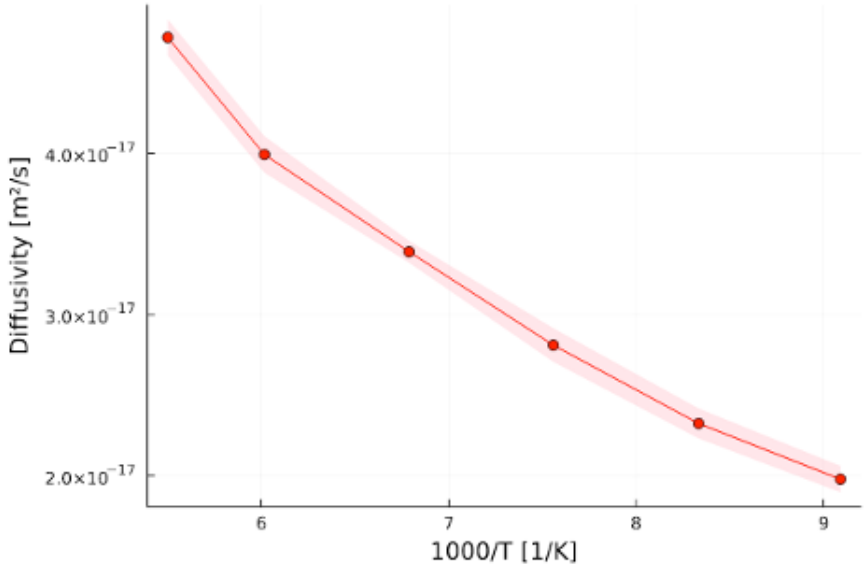

Figure 3. Average diffusivity of carbon atoms in β-SiC obtained from MD simulations performed at temperatures between 1100K and 1818K. The shaded region indicates the standard deviation diffusivity taken from 10 simulations.

2.8. Discussion

Atomistic modeling was utilized in order to build our understanding of the atomic scale phenomena associated with the diffusion of palladium through both graphite and silicon carbide. Molecular dynamics simulations were used to learn more about the fundamental mechanisms governing the transport of Pd atoms at the atomistic scale. Simulation methodologies were developed to compare alternative mechanisms for Pd diffusion and the rates of diffusion for several of these mechanisms were measured using MD simulations. These methodologies were validated in the case of Pd diffusion in graphite, where our model was able to show that diffusion along grain boundaries could result in diffusion rates similar to those in the existing literature. However, the results for determining the primary diffusion mechanism of Pd in SiC were less definitive as multiple mechanisms were energetically feasible. This suggests that the interactions between Pd and SiC are particularly complicated in and around grain boundaries and that simulation methods with higher levels of accuracy such as ab initio MD or density functional theory may be needed to investigate the mechanics of Pd transport at grain boundaries.

Even with these challenges, our simulation work was able to start generating the diffusion parameters for several mechanisms for Pd transport in both graphite and SiC. In particular we were able to obtain the diffusion rates of Pd in SiC via bulk and grain boundary diffusion at a range of temperatures. Additional work was done to measure the diffusion rate of carbon in SiC as a function of temperature. The atomistic modeling work has begun the process of calculating the necessary parameters for higher length scale methods to more accurately model the transport of Pd atoms throughout the TRISO particle.

3. PHASE-FIELD MODEL DEVELOPMENT

3.1. Phase-field model

The phase-field model has been widely used in literature to model the evolution in processes such as solidification, grain growth, and phase separation [12–14]. Discrete microstructural features such as grains and phases are represented using continuous non-conserved variables called order parameter (OP)s, and component atomic fractions are represented using conserved variable fields.

In previous work, a grand-potential-based phase-field model was developed for the Pd-Si-C system. In the grand-potential formulation, the chemical potentials are treated as the independent variables rather than the component atomic fractions. This allows the grand-potential-based phase-field model to control the interface thickness independently of the interface energy [15, 16].

Three phases are considered in the model: graphite, Pd_2Si, and SiC. The other palladium silicide stoichiometries are ignored because Pd_2Si is the most stable at temperatures exceeding 1000°C [17, 18]. The Pd and C chemical potentials are treated as the independent variables in this formulation. The diffusion is then modeled by solving

$$\chi_i \frac{d\mu_i}{dt} = \nabla D_i \chi_i \nabla \mu_i - \sum_j \frac{d\rho_i}{d\eta_j} \frac{d\eta_j}{dt}, \tag{3}$$

where μ_i is the chemical potential of component i, χ_i is the susceptibility, D_i is the diffusivity, ρ_i is the concentration, and η_j is the OP. The concentration of the component can be calculated from

$$\rho_i = \frac{c_i}{V_a}, \tag{4}$$

where V_a is the atomic volume, and c_i is the atomic fraction.

The OPs are evolved by solving the Allen-Cahn equation

$$\frac{d\eta_j}{dt} = -L \frac{d\Omega}{d\eta}, \tag{5}$$

where Ω is the grand-potential of the system and L is the Allen-Cahn mobility for the order parameter η. The grand-potential is computed by applying a Legendre transform to the Helmhholtz free energy. The grand-potential of the system is calculated as

$$\Omega = \int_V (\omega_{chem} + \omega_{int})\, dV, \tag{6}$$

where ω_{chem} and ω_{int} are the chemical and interfacial grand-potential density contributions, and V is the volume of the system. The interfacial grand-potential density contribution is calculated using

$$\omega_{int} = m f_0 + \sum_j \frac{\kappa}{2} |\nabla \eta_j|^2 \tag{7}$$

$$f_0 = \sum_j \left(\frac{\eta_j^4}{4} - \frac{\eta_j^2}{2} \right) + \sum_{k=1}^{p} \sum_{\alpha=1}^{p} \frac{\gamma}{2} \eta_k^2 \eta_\alpha^2 + \frac{1}{4}, \tag{8}$$

where m is the barrier height, κ is the gradient energy coefficient, p is the number of OPs in the system, f_0 is the barrier energy function, and $\gamma = 1.5$ is used so that the OP profiles through the interface are symmetric

[19]. The barrier height and gradient energy coefficients can be computed as functions of the interface energy σ and interface width l using

$$m = \frac{6\sigma}{l}, \tag{9}$$

$$\kappa = \frac{3\sigma l}{4}, \tag{10}$$

allowing us to freely change the interface width of the phase-field model without changing the interface energy [19]. The chemical grand-potential density is interpolated between phases

$$\omega_{chem} = \sum_j h_j \omega_j, \tag{11}$$

where h_j is a switching function that is used to interpolate between the three phases. The model uses a multi-phase switching function that has the form [16, 20]

$$h_j = \frac{\eta_j^2}{\sum_k \eta_k^2}. \tag{12}$$

In previous work, the thermodynamics of the system have been calculated using Computer Coupling of Phase Diagrams and Thermochemistry (CALPHAD) assessments from literature. However, due to very limited experimental data availability, the model used toy diffusivities. In Section 2, we have obtained new predictions of Pd diffusivity in graphite and SiC using MD simulations. These values are used in this work to parameterize the phase-field model kinetics. The values of Pd flux are based on end-of-life Pd flux calculations using BISON, which fall under a separate engineering scale milestone for FY2024. This phase-field model is used to explore the impact of interface energy, Pd flux, and the nature of the flux source on penetration depth and microstructure evolution.

3.2. Effect of interface energy

To understand the impact of the interface energy material property on the lamellar width in the phase-field model, we ran 2D phase-field simulations with interface energies of 2, 4, 8, and 16 J/m^2. It should be noted that 16 J/m^2 is an unphysically large interface energy and is only included to study the model behavior. The lamellar width is found to increase linearly with the interface energy, as shown in figure 4. However, the total penetration depth of Pd into the SiC is found to not change with the interface energy, and only depended on the total mass of Pd added to the system.

3.3. Effect of concentrated Pd source

The IPyC layer in TRISO particles has been known to crack during reactor operation. These cracks are believed to concentrate the flux of FPs compared to the intact IPyC, which could lead to early failure of the SiC layer. The phase-field model is used to simulate the effect of a crack concentrating Pd flux over a small region. A 2D simulation of 1000 nm $\times$ 200 nm in the X and Y directions is set up. As shown in figure 5a, the simulation initially starts with graphite phase in the $X < 100$ nm region, and SiC in the $X > 100$ nm region. Two simulations were run with this same initial condition to simulate the microstructure evolution of SiC exposed to Pd flux over two years. Figure 5b shows the expected lamellar microstructure formation after exposure of the SiC to a uniform Pd flux of 10 pmol/m^2/s over the entire left boundary. Figure 5c shows the

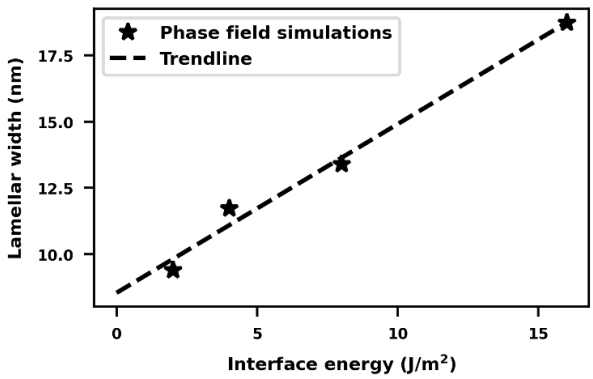

Figure 4. Effect of interface energy on lamellar width of Pd_2Si formed after exposure to a Pd flux of 10 pmol/m^2/s for 2 years.

microstructure evolution when the same initial microstructure is exposed to a flux of 500 pmol/m^2/s through a 4 nm region on the left boundary. The total amount of Pd that enters the system is the same in both cases, and thus the total depth of penetration is the same. However, the concentrated source breaks the uniform lamellar microstructure and leads to the formation of circular graphite phases embedded in the Pd_2Si phase.

3.4. Numerical model development

Development of the damped nested Newton solver for phase-field models that is described in the previous milestone report is completed. The source code, tests and demonstration input files for using the damped nested Newton solver in modeling log-free energies using the Kim-Kim-Suzuki method were pushed to the Multiphysics Object-Oriented Simulation Environment (MOOSE) repository.

The new solver is extended to model the thermodynamics of systems with sublattices. The model builds off previous work on implementing CALPHAD thermodynamics for phase-field models in MOOSE [21]. The nested solver is demonstrated to be able to solve for the evolution of systems with multiple sub-lattice concentrations. As an example, the four component Chromium-Molybdenum-Nickel-Rhenium system consisting of four phases - BCC, FCC, σ, and HCP, is chosen. Of these, the σ-phase consists of five sublattices. Thus, a total of 24 concentration variables is solved for by the nested Newton solver. Figure 6 shows the results of solving the Allen-Cahn equation for the calculation of the phase-diagram by varying the atomic fractions of Ni, Re and Mo with a constant Cr atomic fraction of 10^{-12}.

3.5. Discussion

The Pd penetration depth in SiC is found to be independent of the interface energy, and whether the flux source is uniform or concentrated, such as from a crack in the IPyC layer. Instead, it depends solely on the total Pd mass added to the system, a finding that will be utilized in the following section to develop a ROM for Pd penetration depth in BISON. The lamellar width of the Pd_2Si-graphite microstructure is found to be linearly proportional to the interface energy. This is because the interface energy serves as the energy barrier for the nucleation of a new lamellar layer, so for the same amount of Pd, fewer layers develop. Similarly, while the nature of the Pd flux does not change the penetration depth, uniform Pd flux leads to the formation of lamellar microstructures, while concentrated sources of Pd flux lead to the formation of circular graphite phase particles

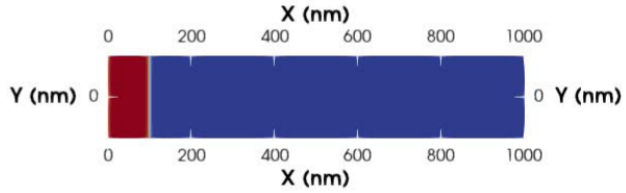

(a)

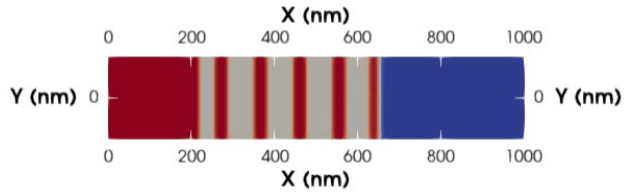

(b)

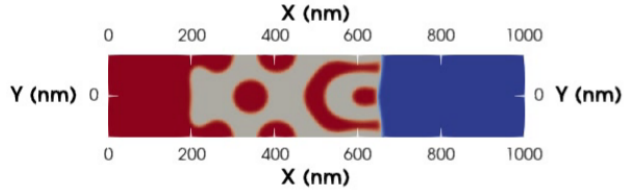

(c)

Figure 5. Effect of uniform and concentrated Pd flux sources on microstructure evolution of SiC. The red region denotes graphite phase, blue region denotes SiC, and the gray region denotes Pd_2Si. (a) Initial microstructure consists of SiC with an initial 100 nm layer of graphite (red). (b) Final microstructure (t=2 years) after a uniform Pd flux of 10 pmol/m^2/s on the left boundary. (c) Final microstructure (t=2 years) after a concentrated Pd flux of 500 pmol/m^2/s through a 4 nm region on left boundary.

embedded in a Pd_2Si matrix. This corresponds with experimental observations, where uniform Pd plating leads to the formation of lamellar layers, but the Pd_2Si layers also have embedded carbon nanoparticles [22]. This is likely due to the imperfections of real materials, while phase-field simulates the SiC as completely free of defects.

The newly implemented damped nested Kim-Kim-Suzuki (KKS) capability in MOOSE enables the simulation of more complex systems. By directly solving the actual system thermodynamics, this capability eliminates the need for polynomial approximations of free energy, leading to more accurate and reliable results. The damped nested solver capability is utilized for simulating phase evolution of a complex four component, four phase system with five sublattices. This capability will enable simulation of complex interactions between Ag and Pd leading to accelerated liquid phase attack at higher temperatures in the future.

During the development of a phase-field model for Pd attack of SiC, an increase in the number of nucleated lamellae is observed with increasing phase-field interface width (l) for a given amount of Pd. This behavior stems from a numerical instability in the Allen-Cahn equation at high interface velocities, a phenomenon documented in the literature [23–25]. The stability of the Allen-Cahn equation is governed by the ratio of the driving force for interface movement (ω_{chem}) to the driving force for stabilizing the interface, $\mu_{int} = 6\sigma/l$.

Thus the stability criterion can be written out as

$$\frac{6\sigma}{l} > C\omega_{chem}, \tag{13}$$

where C is a factor dependent on the switching function used in the phase-field model [23–25]. If this condition is satisfied, the phase-field model's stabilizing force in the bulk phases surpasses the driving force for the evolution of a new phase. This prevents unphysical phase evolution within the bulk. However, as the interface width of the phase-field model increases, the stabilizing force for the interface diminishes. To accurately model high-temperature attack of liquid-phase Pd at the mesoscale, this stabilization issue must be resolved. Although several straightforward approaches to mitigate this problem have been proposed in the literature, none are currently implemented in MOOSE. To circumvent these limitations, phase-field simulations were run with small interface widths to understand the solid state attack of Pd in the bulk of SiC grains. Studying GB effects as well as high temperature liquid phase attack of Pd-Ag will require implementation of a numerical stabilization approach for the Allen-Cahn equation in MOOSE.

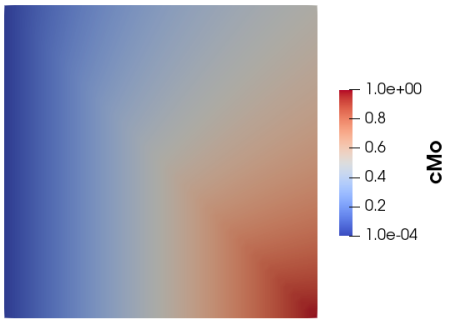

(a)

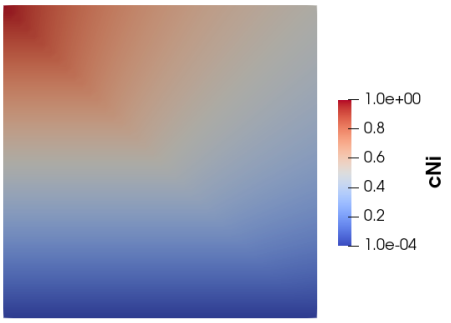

(b)

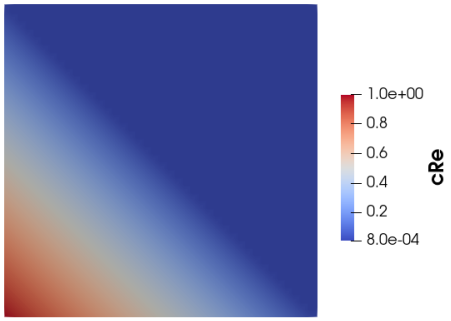

(c)

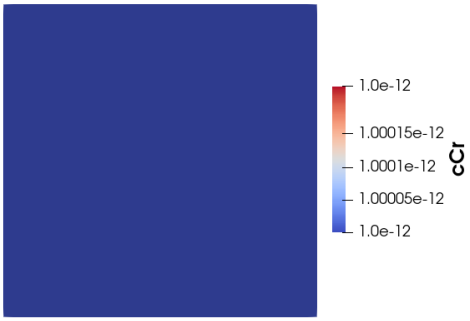

(d)

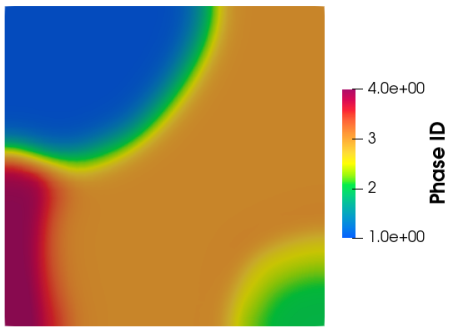

(e)

Figure 6. Phase diagram calculation for Mo-Ni-Re-Cr system using the sub-lattice Kim-Kim-Suzuki phase-field model implemented using the damped nested solver in MOOSE. (a)-(d) show the atomic fractions of the components. (e) shows the stable phases calculated based on the composition and interface energy by solving the Allen-Cahn equation based on the local composition. Phase IDs 1,2,3,4 signify the phases FCC, BCC, σ, and HCP each respectively.

4. ENGINEERING SCALE REDUCED ORDER MODEL DEVELOPMENT

4.1. Derivation of mechanistic reduced order model

The mesoscale model presented in section 3 shows that the penetration depth rate of Pd does not depend on any material properties except Pd flux due to the high driving force for phase transformation. Based on this, at any given location on the inner surface of the SiC, the penetration depth rate is

$$\frac{dP_{Pd}}{dt} = 3V_m J_{Pd}(t), \tag{14}$$

where $J_{Pd}(t)$ is the Pd flux at time t, V_m is the molar volume of SiC, and $\frac{dP_{Pd}}{dt}$ is the Pd penetration depth rate. The factor 3 arises from the phase-field model's assumption that diffusion of two atoms of Pd into the SiC implicitly removes two Si atoms by lattice substitution. The Pd-SiC reaction then consumes a further four reactant atoms (two Pd, one Si and one C). Thus for every atom of Pd, three atomic volumes worth of SiC is reacted to form Pd_2Si and C.

The Pd flux supplied by BISON is an average value over the entire IPyC-SiC interface region. However, Pd transport is faster along SiC GBs compared to the bulk. This should cause the Pd flux at GBs to be higher than in the bulk. Since Pd penetration depth is measured experimentally by finding the farthest locations (radially) in the SiC with detectable Pd concentrations, this biases the penetration depth to depend primarily on the Pd flux at GBs. The penetration depth rate is then

$$\frac{dP_{Pd}}{dt} = \frac{3V_m f}{0.5\pi} J_{Pd}(t), \tag{15}$$

where f is the flux enhancement factor, given by $f = J_{Pd}^{GB} / J_{Pd}^{0}$, and J_{Pd}^{0} is the average Pd flux at the IPyC/SiC interface calculated by BISON. The flux enhancement factor calculated in section4.2 assumes rectangular parallelopiped grains. In reality, grains have a much more complicated shape, which is approximated as spherical for calculating the penetration depth. Thus, when the Pd travels the distance of half the circumference of the grain, the penetration depth equals the diameter of the grain. To account for this, the flux enhancement factor is divided by 0.5π.

Further, due to the sphericity of the TRISO particle, the Pd flux becomes more diffuse as the Pd penetrates deeper into the SiC. Thus, the flux from BISON needs to also be scaled based on the Pd penetration depth as

$$J_{Pd} = J_{Pd}^{0} \left(\frac{r_{SiC}}{r_{SiC} + P_{Pd}(t)} \right)^2. \tag{16}$$

This scales the Pd flux based on the ratio of the initial area over which BISON calculates the Pd flux, to the area of the sphere represented by the Pd penetration depth front. Substituting into Equation (15)

$$\frac{dP_{Pd}}{dt} = \frac{6V_m f}{\pi} J_{Pd}^{0} \left(\frac{r_{SiC}}{r_{SiC} + P_{Pd}(t)} \right)^2. \tag{17}$$

The terms can be shuffled around to separate the variables as

$$(r_{SiC} + P_{Pd})^2 \, dP_{Pd} = \frac{6V_m f r_{SiC}^2}{\pi} J_{Pd}^{0} dt. \tag{18}$$

Integrating both sides yields

$$\frac{(r_{SiC} + P_{Pd})^3}{3} P_{Pd} = \frac{6V_m f r_{SiC}^2}{\pi} \int_{t=0}^{t} J_{Pd}^{0} dt + C, \tag{19}$$

where C is the constant of integration. Solving for P_{Pd} yields

$$P_{Pd}(t) = \sqrt[3]{\frac{18V_m f r_{SiC}^2}{\pi} \int_{t=0}^{t} J_{Pd}(t)dt + r_{SiC}^3} - r_{SiC}, \tag{20}$$

where the integration constant $C = r_{SiC}^3$ is chosen to ensure that $P_{Pd} = 0$ when $\int_{t=0}^{t} J_{Pd}(t)dt = 0$.

4.2. Calculation of flux concentration factor

This sub-section details the derivation of the flux enhancement factor used in section 4.1. The grains are assumed to be rectangular parallelepiped grains with a minor axis size m_i and major axis size m_a. Based on experimental observations of SiC microstructure, the major axis of the grains is assumed to be along the radial direction of the TRISO particle, and the minor axis is along the tangential direction. Thus, the major axis is parallel to the direction of the Pd flux.

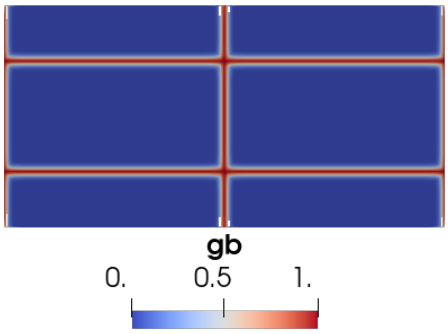

(a)

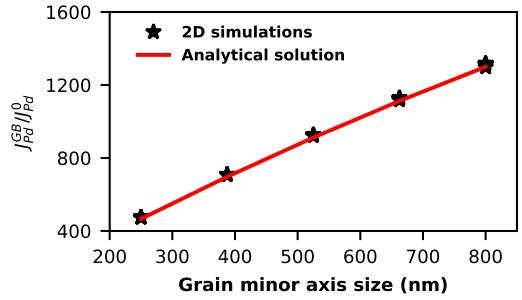

(b)

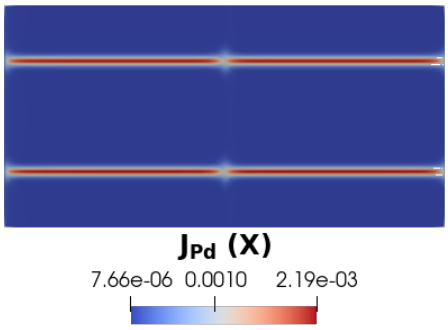

(c)

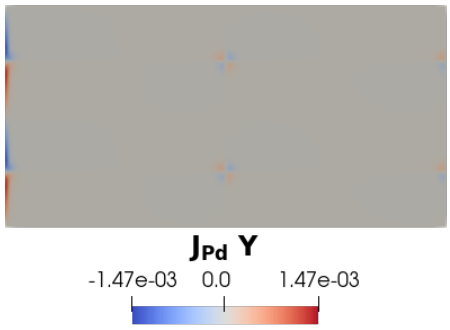

(d)

Figure 7. Comparison of 2D diffusion simulation results against analytical expression for flux enhancement factor f. (a) shows the grain boundaries, as indicated by the value of the variable GB, used to interpolate Pd diffusivity in the 2D simulations. (b) compares the results of the steady state diffusion simulation and analytical solution values for f against the grain minor axis size m_i. The 2D simulation points include five values of grain major axis size m_a for each value of m_i, but the points overlap due to the negligible impact of m_a on f. The root mean square percentage error (RMSPE) between the analytical expression and 2D simulation results is 1.4%. (c) and (d) show the steady-state Pd flux along the x and y directions respectively. The flux is higher along the GBs in the x axis than the grains, and is negligible along the y direction far from the left boundary.

To inform an analytical model for the flux enhancement factor, a 2D diffusion simulation was set up using MOOSE with enhanced diffusion along the GB. As shown in figure 7a, two grain boundaries are generated in the x and y directions each, such that the rectangular grains formed by their intersection has the grain size $m_a \times m_i$ nm^2. Each grain is represented by an order parameter η_i which has a value of 1 inside grain i and 0 for grains $j \neq i$, with a diffuse interface between 0 and 1 representing the grain boundary. The variable $GB = 16\eta_i^2\eta_j^2$ is defined to indicate the position of grain boundaries; $GB = 1$ at grain boundaries and $GB = 0$ in grain interiors. A constant Pd flux is applied on the left boundary using a Neumann boundary condition (BC), and a Dirichlet BC enforcing a Pd atomic fraction of zero is applied on the right boundary. The steady-state solution to the diffusion equation is then solved. The ratio of the average flux along the GBs parallel to the x direction to the applied constant flux at the left boundary is used to calculate the flux enhancement factor f. The diffusivity of Pd is interpolated based on the GB value

$$D_{Pd} = D_{Pd}^{bulk} + 1.5GB\frac{l}{d_{GB}}(D_{Pd}^{GB} - D_{Pd}^{bulk}), \tag{21}$$

where $d_{GB} = 0.5$ nm is the GB width, $l = 25$ nm is the phase-field interface width, and D_{Pd}^{bulk} and D_{Pd}^{GB} are the Pd diffusivities in the grain bulk and GB. The diffusivity values are taken from the MD calculation results in Table 2. The 1.5 scaling factor is added to correct the diffuse interface width to an equivalent sharp interface width. The simulation mesh size is set to ensure that there are 8 elements across the GB.

A grid sampling study is run for various values of m_i and m_a to study the impact of each parameter on the f. The values of m_i are 250, 387.5, 525, 662.5 and 800 nm, and the values of m_a are 500, 1125, 1750, 2375, and 3000 nm. This value range is based on the observed grain size range in the AGR-1 and AGR-2 TRISO particles [2, 26]. The results of this sampling study indicated that the effect of the major axis size m_a on f was found to be negligible. The relationship between m_i and f is shown in figure 7b. In the grid sampling study, for each value of m_i, five values of m_a are sampled, and their values are also plotted in the same figure. However, the variations in m_a make no impact on the flux enhancement factor, and the points completely overlap in the plot. Additionally, as seen from Figure 7d, the Pd diffusion flux in the grains and GB is zero in the y direction everywhere except very close to the left boundary.

This information is used to build an analytical expression for the flux enhancement factor in terms of the minor axis size, Pd diffusion coefficients, and GB width. For 2D grains, the total flux received N grains at the IPyC/SiC interface is $Nm_iJ_{Pd}^0$. This flux is divided between N GBs and the bulk of the grains. As the flux in the y direction is zero, the gradient of the atomic fraction of Pd has to be zero in the y-direction. This requires that the Pd atomic fraction is constant in the y-direction for any given value of x. Thus,

$$\frac{dc_{Pd}^{GB}}{dx} = \frac{dc_{Pd}^{bulk}}{dx} \tag{22}$$

Then the total flux is given by

$$Nm_iJ_{Pd}^0 = Nd_{GB}D_{Pd}^{GB}\frac{dc_{Pd}^{bulk}}{dx} + (Nm_i - Nd_{GB})D_{Pd}^{bulk}\frac{dc_{Pd}^{bulk}}{dx}. \tag{23}$$

The concentration gradient can be solved for using

$$\frac{dc_{Pd}^{bulk}}{dx} = \frac{m_iJ_{Pd}^0}{d_{GB}D_{Pd}^{GB} + (m_i - d_{GB})D_{Pd}^{bulk}}. \tag{24}$$

The flux in the GB is written as

$$J_{Pd}^{GB} = \frac{m_iD_{Pd}^{GB}}{d_{GB}D_{Pd}^{GB} + (m_i - d_{GB})D_{Pd}^{bulk}}J_{Pd}^0. \tag{25}$$

Thus the flux enhancement factor f can be written as

$$f = \frac{m_i D_{Pd}^{GB}}{d_{GB} D_{Pd}^{GB} + (m_i - d_{GB}) D_{Pd}^{bulk}}. \tag{26}$$

Figure 7b shows the comparison of the 2D analytical expression against the 2D diffusion simulations. The results match well, with a root mean square percentage error (RMSPE) of 1.4%.

Similarly, in 3D, the total flux received by a grid of $N \times N$ grains at the IPyC/SiC interface can be written as

$$N^2 m_i^2 J_0^{Pd} = \left[2N^2 m_i d_{GB} D_{Pd}^{GB} + (N^2 m_i^2 - 2N^2 m_i d_{GB}) D_{Pd}^{bulk}\right] \frac{dc_{Pd}}{dx}. \tag{27}$$

Removing $N^2 m_i$ from both sides yields

$$m_i J_0^{Pd} = \left[2 d_{GB} D_{Pd}^{GB} + (m_i - 2 d_{GB}) D_{Pd}^{bulk}\right] \frac{dc_{Pd}}{dx}. \tag{28}$$

The 3D flux enhancement factor can be derived as

$$f = \frac{m_i D_{Pd}^{GB}}{2 d_{GB} D_{Pd}^{GB} + (m_i - 2 d_{GB}) D_{Pd}^{bulk}}. \tag{29}$$

The BISON ROM uses the flux enhancement factor calculated for 3D grains. The 2D grain flux enhancement factor underestimates the GB coverage at the IPyC/SiC interface, leading to an overestimation of the penetration depth. This flux enhancement factor is used in calculating the Pd penetration depth using Equation (20).

4.3. Validation of ROM

The expression for calculating the Pd penetration depth was implemented using ParsedPostprocessors and TimeIntegratedPostprocessor in a BISON input file. The Pd flux at the IPyC/SiC interface is calculated as a function of the particle temperature and burnup history. The details of the calculation of the Pd flux are part of a separate engineering scale fission product release milestone and will be described in a different report. This work uses the Pd flux calculations to implement the ROM and compare it against experimental data for Pd penetration depth.

The experimental data points used for validation are generated from a plot re-digitization of figure 3-68 from an INL report that combines data from multiple experimental reports and papers [27–31].

For comparison against the experimental data, a BISON simulation was set up to achieve 13.15% burnup in 560 days, mimicking AGR-2 Compact 2-4-2 [32]. The Pd flux dependent penetration depth ROM was implemented into the BISON input script using the MOOSE postprocessor system. A Python script was then written to perform a sampling study on the BISON input file, varying the surface temperature and minor axis grain size of the simulation. The BISON script uses Equation (20) and 29 to account for the effect of the grain size on the Pd penetration depth. The surface temperature was sampled by varying the temperature inverse ($10^4 / T_{surf}$) between 4-9. The grain minor axis values are sampled in the same range that is used during the flux concentration factor simulations in section 4.2.

To calculate the average rate of Pd penetration, the final penetration depth was divided by the simulation time, to calculate the rate in μm/hr. The results of the sampling study are plotted along-with the re-digitized points in figure 8.

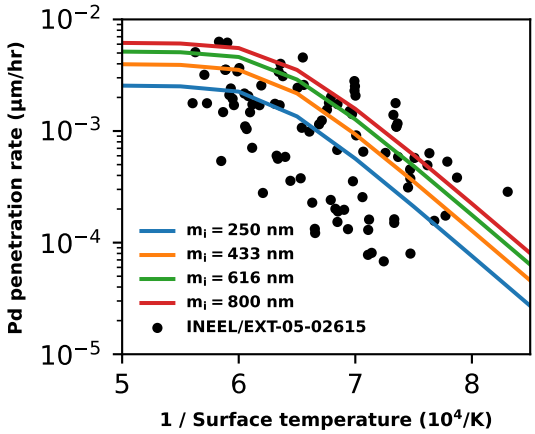

Figure 8. Effect of surface temperature and grain minor axis length m_i on Pd penetration depth rate.

4.4. Comparison to empirical BISON model

This section compares the microstructure-informed mechanistic ROM developed in this work against the existing empirical model for Pd penetration in BISON. The empirical model for Pd penetration rate in BISON is generated from an Arrhenius curve fitted to this experimental data. It is given as

$$\dot{P_{Pd}} = 38.232 \exp \frac{-11342.3}{T_K}, \tag{30}$$

where $\dot{P_{Pd}}$ is the rate of penetration of Pd into the SiC layer in μm/day, and T_K is the temperature of the SiC. The total Pd penetration depth is then calculated by performing a trapezoidal rule time integration of the rate. This expression solely depends on the SiC temperature and does not account for burnup, which is what actually produces the Pd.

To compare the mechanistic and empirical ROM predictions, a transient operation 1D simulation was run for a single TRISO particle using BISON. The power and temperature conditions applied to the TRISO particle are shown in figure 9a. The particle initially starts at a temperature of 1273 K, and is cooled down to room temperature (298.15 K) linearly over the course of a year starting from three years. The particle power density is zero initially, and is raised to 2.03 GW/m^3 between years one to two. After year two, the power is brought back down to zero for the remainder of the simulation.

Figure 9b presents a comparison of empirical and mechanistic ROMs. As expected from Equation (30), the empirical ROM predicts a linear increase in the Pd penetration depth in SiC till year three, since the surface temperature is held at 1273 K. As the temperature drops to room temperature, the rate of penetration depth increase drops down to zero, and reaches a maximum value of about 5.9μm. In contrast, the mechanistic ROM shows zero penetration depth until year one. Between year one and two, the Pd penetration depth increases non-linearly. The penetration depth rate decreases after the particle power becomes zero again at two years. As the surface temperature ramps down, the mechanistic ROM predicts a further drop in the penetration depth rate. After five years, the mechanistic ROM predicts a final penetration depth of around 1.7μm.

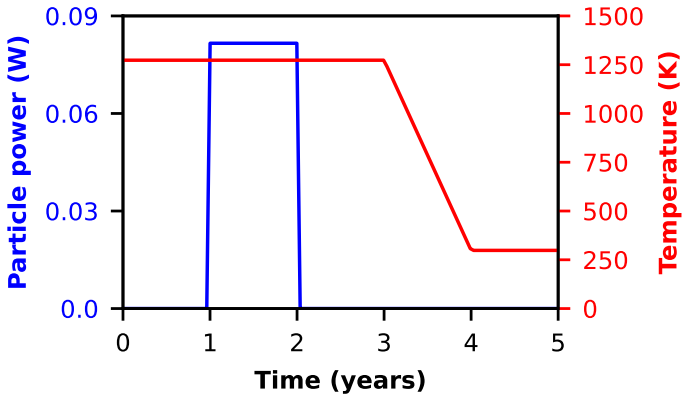

(a)

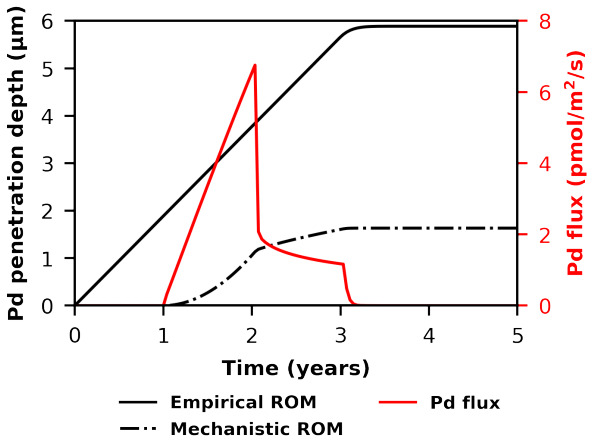

(b)

Figure 9. Comparison of Pd penetration depth prediction over time between empirical fit and mechanistic ROM. (a) Particle power and temperature conditions simulated using BISON (b) Pd flux at IPyC/SiC boundary calculated by BISON, and comparison of empirical and mechanistic ROM penetration depths over time. The empirical ROM predictions only depend on the particle temperature, while the mechanistic ROM predicts a penetration depth dependent on both the particle power history and temperature.

4.5. Discussion

This section presented the development of a mechanistic ROM to predict Pd penetration in TRISO particles. The model accounts for the effects of burnup history, particle temperature, and SiC microstructure. The model's predictions provide a conservative upper bound for experimentally observed Pd penetration depth rates. Equation (20) predicts that the penetration depth is proportional to the cube root of the mass of palladium that has diffused into the SiC, which matches the conservative upper bound fit made to experimental data in literature [29]. Additionally, faster deposition rate of the SiC layer is observed to result in columnar grains with higher penetration depth rates in experiments [31]. This effect is again captured by the mechanistic ROM's dependence on grain minor axis size.

However, the model's results are sensitive to the chosen palladium diffusivity in the fuel kernel, with

significant differences in Pd penetration depth based on whether experimental or MD diffusivities were used. Future work should focus on more accurately quantifying Pd diffusivity in the fuel kernel based on the kernel composition and microstructure. It's important to note that the experimental data points in figure 8 originate from various experiments with different setups, which likely contribute to the large scatter in experimental observations. The experiments from which the data points in this validation were obtained used un-irradiated particles with fuel doped with FPs [31], high temperature irradiation for fuel with varying initial U-235 enrichment and burnup rates [29], and irradiation at low temperatures followed by heating in a furnace [30]. To further validate the model and demonstrate that it can capture the full data scatter, future work should involve replicating individual experimental conditions using BISON. Finally, the ROM should be applied to 2D and 3D spatially resolved TRISO fuel models to include the effect of IPyC layer cracking on Pd flux concentration.

5. CONCLUSION

In this work, a ROM for predicting Pd penetration depth in the SiC layer of TRISO particles was developed. This included atomistic scale calculations of temperature dependent diffusivity of Pd in graphite and SiC using MD simulations. The capability to calculate C diffusivity in SiC using MD was also demonstrated. The calculated diffusivities were used to parameterize both the mesoscale phase-field model and the engineering scale ROM. The phase-field model was used to demonstrate that due to the large driving force for the reaction of Pd with SiC to form Pd_2Si, the penetration depth of Pd into bulk SiC depends primarily on the flux received at the IPyC/SiC boundary. The interface energy impacts the lamellar width of the microstructure of Pd_2Si/graphite, and heterogeneity in the Pd flux can drive the formation of spherical graphitic particles instead of the lamellar microstructure observed with a homogeneous flux. The results of this mesoscale model were also used to inform the mechanistic BISON ROM.

A mechanistic expression for the Pd penetration depth was derived as a function of the flux produced via fission, SiC microstructure, particle temperature and geometry. This expression was then implemented in a BISON input file to calculate penetration depth rate under varying conditions of particle surface temperature and SiC microstructure. The model was then validated against experimental data for average Pd penetration depth rates. The model predictions are in good agreement with the experimental data, providing an upper bound for the penetration depth rate. This makes the model well suited for identifying safe operating parameters for TRISO fuels in advanced reactor designs.

However, the ROM still does not capture the full spread of experimental data points, which spans almost two orders of magnitude. Future work should include a more thorough validation that involves replicating the various experimental conditions to build more confidence in the model predictions. An improved understanding of the high temperature liquid-phase attack of Pd-Ag is also required to better parameterize the impact of the SiC microstructure on the penetration depth, as well as understand the microstructural changes during Pd attack and how they affect FP release. High fidelity atomistic modeling, ab initio MD, will be utilized to investigate the interactions between Pd atoms and SiC grain boundaries to validate the high temperature liquid-phase mechanism of attack of Pd on SiC. Atomistic modeling will also assist in parameterizing the conditions and rates at which this process occurs in order to help improve the accuracy of higher length scale models.

6. REFERENCES

[1] J. D. Hales, W. Jiang, A. Toptan, and K. A. Gamble, "Modeling fission product diffusion in triso fuel particles with bison," *Journal of Nuclear Materials*, vol. 548, p. 152840, 2021.

[2] P.-C. Simon, L. K. Aagesen, C. Jiang, W. Jiang, and J.-H. Ke, "Mechanistic calculation of the effective silver diffusion coefficient in polycrystalline silicon carbide: Application to silver release in agr-1 triso particles," *Journal of Nuclear Materials*, vol. 563, p. 153669, 2022.

[3] T. Lillo and I. van Rooyen, "Associations of pd, u and ag in the sic layer of neutron-irradiated triso fuel," *Journal of Nuclear Materials*, vol. 460, p. 97–106, May 2015.

[4] I. van Rooyen, T. Lillo, and Y. Wu, "Identification of silver and palladium in irradiated triso coated particles of the agr-1 experiment," *Journal of Nuclear Materials*, vol. 446, p. 178–186, Mar. 2014.

[5] H. Wen and I. J. van Rooyen, "Distribution of fission products palladium, silver, cerium and cesium in the un-corroded areas of the locally corroded sic layer of a neutron irradiated triso fuel particle," *Journal of the European Ceramic Society*, vol. 37, p. 3271–3284, Aug. 2017.

[6] P.-C. A. Simon, L. K. Aagesen, Jr., C. V. Bhave, C. Jiang, W. Jiang, J.-H. Ke, and L. Yang, "Multi-scale fission product release model with comparison to agr data," 6 2023.

[7] A. P. Thompson, H. M. Aktulga, R. Berger, D. S. Bolintineanu, W. M. Brown, P. S. Crozier, P. J. in 't Veld, A. Kohlmeyer, S. G. Moore, T. D. Nguyen, R. Shan, M. J. Stevens, J. Tranchida, C. Trott, and S. J. Plimpton, "LAMMPS - a flexible simulation tool for particle-based materials modeling at the atomic, meso, and continuum scales," *Computer Physics Communications*, vol. 271, p. 108171, 2022.

[8] P. Hosemann, J. Martos, D. Frazer, G. Vasudevamurthy, T. Byun, J. Hunn, B. Jolly, K. Terrani, and M. Okuniewski, "Mechanical characteristics of sic coating layer in triso fuel particles," *Journal of Nuclear Materials*, vol. 442, no. 1, pp. 133–142, 2013.

[9] P. Hirel, "Atomsk: A tool for manipulating and converting atomic data files," *Computer Physics Communications*, vol. 197, pp. 212–219, 2015.

[10] N. Chen, Q. Peng, Z. Jiao, I. van Rooyen, W. F. Skerjanc, and F. Gao, "Analytical bond-order potential for silver, palladium, ruthenium and iodine bulk diffusion in silicon carbide," *Journal of Physics: Condensed Matter*, vol. 32, p. 085702, nov 2019.

[11] T. Weilert, K. Walton, S. Loyalka, and J. Brockman, "Effective diffusivity of ag and migration of pd in ig-110 graphite," *Journal of Nuclear Materials*, vol. 559, p. 153427, 2022.

[12] L.-Q. Chen, "Phase-field models for microstructure evolution," *Annual Review of Materials Research*, vol. 32, pp. 113–140, Aug. 2002.

[13] N. Moelans, B. Blanpain, and P. Wollants, "An introduction to phase-field modeling of microstructure evolution," *Calphad*, vol. 32, pp. 268–294, June 2008.

[14] M. R. Tonks and L. K. Aagesen, "The phase field method: mesoscale simulation aiding material discovery," *Annual Review of Materials Research*, vol. 49, pp. 79–102, 2019.

[15] M. Plapp, "Unified derivation of phase-field models for alloy solidification from a grand-potential functional," *Physical Review E*, vol. 84, no. 3, 2011.

[16] L. K. Aagesen, Y. Gao, D. Schwen, and K. Ahmed, "Grand-potential-based phase-field model for multiple phases, grains, and chemical components," *Physical Review E*, vol. 98, no. 2, 2018.

[17] Z. Du, C. Guo, X. Yang, and T. Liu, "A thermodynamic description of the pd–si–c system," *Intermetallics*, vol. 14, pp. 560–569, May 2006.

[18] C. Jiang, I. J. van Rooyen, and S. Meher, "Ab initio study and thermodynamic modeling of the pd-si-c system," *Computational Materials Science*, vol. 171, p. 109238, Jan. 2020.

[19] N. Moelans, B. Blanpain, and P. Wollants, "Quantitative analysis of grain boundary properties in a generalized phase field model for grain growth in anisotropic systems," *Physical Review B*, vol. 78, no. 2, 2008.

[20] N. Moelans, "A quantitative and thermodynamically consistent phase-field interpolation function for multi-phase systems," *Acta Materialia*, vol. 59, pp. 1077–1086, Feb. 2011.

[21] D. Schwen, C. Jiang, and L. Aagesen, "A sublattice phase-field model for direct calphad database coupling," *Computational Materials Science*, vol. 195, p. 110466, 2021.

[22] H. Liu, Y. Chen, Z. Gao, N. Rohbeck, and P. Xiao, "A study of reaction between palladium, palladium silver alloy and silicon carbide ceramics at high temperature," *Journal of the European Ceramic Society*, vol. 43, pp. 3077–3089, July 2023.

[23] V. Feyen and N. Moelans, "Quantitative high driving force phase-field model for multi-grain structures," *Acta Materialia*, vol. 256, p. 119087, 2023.

[24] C. J. Grose and P. D. Asimow, "A multi-phase field model for mesoscopic interface dynamics with large bulk driving forces," *Computational Materials Science*, vol. 212, p. 111570, 2022.

[25] J. Zhang, A. F. Chadwick, D. L. Chopp, and P. W. Voorhees, "Phase field modeling with large driving forces," *npj Computational Materials*, vol. 9, Sept. 2023.

[26] T. J. Gerczak, J. D. Hunn, R. A. Lowden, and T. R. Allen, "Sic layer microstructure in agr-1 and agr-2 triso fuel particles and the influence of its variation on the effective diffusion of key fission products," *Journal of Nuclear Materials*, vol. 480, pp. 257–270, 2016.

[27] D. Petti, P. Martin, M. Phelip, and R. Ballinger, "Development of improved models and designs for coated-particle gas reactor fuels – final report under the international nuclear energy research initiative (i-neri)," 12 2004.

[28] T. N. Tiegs, "Fission product pd-sic interaction in irradiated coated-particle fuels," *Nuclear Technology*, vol. 57, no. 3, pp. 389–398, 1982.

[29] K. Minato, T. Ogawa, S. Kashimura, K. Fukuda, M. Shimizu, Y. Tayama, and I. Takahashi, "Fission product palladium-silicon carbide interaction in htgr fuel particles," *Journal of Nuclear Materials*, vol. 172, no. 2, pp. 184–196, 1990.

[30] F. Montgomery, "Fission-product sic reaction in htgr fuel," 7 1981.

[31] R. Lauf, T. Lindemer, and R. Pearson, "Out-of-reactor studies of fission product-silicon carbide interactions in htgr fuel particles," *Journal of Nuclear Materials*, vol. 120, no. 1, pp. 6–30, 1984.

[32] J. D. Stempien, J. D. hunn, R. N. Morris, T. J. Gerczak, and P. A. Demkowicz, "Agr-2 triso fuel post-irradiation examination final report," 9 2021.